

Influence and Electrochemical Stability of Oxygen Groups and Edge Sites in Vanadium Redox Reactions

Hannes Radinger, Jessica Pfisterer, Frieder Scheiba,* and Helmut Ehrenberg^[a]

It is widely accepted that surface-active oxygen functional groups (OFGs) effectively catalyze the vanadium redox reactions. Initial graphitic edge sites, OFGs and their electrochemical stability were examined using graphite felts, which were modified with multi-walled carbon nanotubes and activated with KOH. It is demonstrated that OFGs cannot exclusively be responsible for the electrocatalysis since they did not correlate to the electrochemical activity. The surface composition after electrochemical cycling in the positive half-cell was still different for all samples but did not reflect the performance either.

However, a correlation was found between the activity and stable edge site defects. There was neither a correlation between the electrocatalytic activity and the amount of oxygen, nor for the kind of OFG in the negative half-cell. The oxygen concentration after electrochemistry was very similar, even more highlighting the importance of edge sites in the V^{III}/V^{II} redox reaction. The results of this work indicate that the major electrocatalytic effect for both half-cell redox reactions is related to stable graphitic edge sites in sufficient quantity.

1. Introduction

For many electrochemical applications that utilize graphitic materials such as batteries, electrolyzers, or supercapacitors, surface-active oxygen functional groups (OFGs) at the electrode are considered essential.^[1–3] It is widely accepted that OFGs work as an effective catalyst towards the occurring redox reactions in a vanadium flow battery (VFB).^[4–7] This has sparked a lot of scientific as well as industrial activities, which focus on the optimization of the carbon-based electrodes by various oxidative treatments. Several surface treatment methods have been reported to increase the activity of the felt electrode by employing OFGs using thermal, chemical, electrochemical, acid or alkaline activation.^[8–12] The mere amount of studies may explain why literature is sometimes contradictory in the results, especially when the material characterization after the respective surface treatment is directly related to the electrochemical activity. Most of the used oxidative treatments are as well expected to damage the material and create graphitic defects in the form of edge sites.


A clear discrimination between graphitic OFGs that appear on basal and edge planes, and defects (such as edge sites) is difficult and thus the observed activity can hardly be attributed to one specific property. For instance, Kim *et al.* modified their electrode with H_2O_2 after the formation of free radical bonds by a corona discharge to increase the number of OFGs.^[13] They

stated a significant increase of the $V^{VO_2^+}/V^{VO^{2+}}$ half-cell performance and ascribed this fully to the formation of additional oxygen groups. However, in a prior study the same authors declared that several oxidative treatments significantly increased the number of OFGs, which resulted in almost no positive effect on the battery performance.^[14] In another study the authors observed increased activity in both half-cells after the introduction of hydroxyl groups by treating paper electrodes with a mixture of concentrated sulfuric and nitric acid.^[10] In a further study H_2O_2 in combination with an oxygen plasma treatment was used to increase the activity of a full cell.^[15] In this article, O=C–OH groups are reported to enhance the activity, whereas O=C and O=C had a negative effect. Elsewhere, the electrochemical oxidation of glassy carbon led to enhanced reduction kinetics.^[16] The authors explained this with the formation of catalytically active hydroxyl groups.

Most reported methods probably lead to the formation of surface graphitic edge sites. However, the electrocatalytic role of defects is discussed to a lower degree in literature. In previous studies of edge and basal plane exposed highly oriented pyrolytic graphite it was shown in general that edge sites provide faster electron transfer for redox reactions.^[17] It was specifically demonstrated that the kinetics of the vanadium redox reactions are enhanced by increasing the number of edge sites.^[18] Furthermore it was reported that there is a difference in the electrocatalytic activity between oxygenated defects at the graphite edges and in the basal plane.^[19] The authors conclude that the activity towards the vanadium redox couples is dependent on OFGs on edges and a well-preserved basal plane. Similar results were obtained by another group, which found active OFGs that are only stable on edge sites, to catalyze the V^{III}/V^{II} redox reaction.^[20]

However, even more questions towards surface functional groups seem to arise when carbon-based nanomaterials such as graphene or multi-walled carbon nanotubes (MWCNTs) are investigated. The activity of MWCNTs has been examined and it

[a] H. Radinger, J. Pfisterer, Dr. F. Scheiba, Prof. H. Ehrenberg
Institute for Applied Materials
Karlsruhe Institute of Technology
Hermann-von-Helmholtz-Platz 1,
76344 Eggenstein-Leopoldshafen, Germany
E-mail: frieder.scheiba@kit.edu

 © 2020 The Authors. ChemElectroChem published by Wiley-VCH GmbH. This is an open access article under the terms of the Creative Commons Attribution Non-Commercial License, which permits use, distribution and reproduction in any medium, provided the original work is properly cited and is not used for commercial purposes.

was concluded that they have no intrinsic catalytic effect on the $V^{VO_2^+}/V^{VO_2^{2+}}$ redox pair.^[21,22] Prior treatment to increase the activity is therefore widely considered in the form of hydroxylation or carboxylation, attachment of functional groups, sulfonating, or heteroatom doping.^[23–29] Similar to the treatment of graphitefelt electrodes, these procedures are expected to damage the graphitic basal plane, which consequently introduces edge sites. Therefore, the real activity enhancement of the treatment is hard to separate from the pure addition of active edge sites.

In this work, we try to disentangle the respective role of OFGs and edge sites towards the electrocatalysis of graphite felt electrodes in VFBs. Owing to their intact sp^2 structure and wide modification potential, MWCNTs serve as a good substrate to study the influence of surface defects in more detail. Ready-made pristine MWCNTs were attached to graphite felt. A KOH activation treatment was chosen to effectively create edge sites and introduce OFGs on the material. This resulted in a set of four samples with different defect density and relative surface oxygen content. We investigated the sample morphologies by Scanning Electron Microscopy (SEM), the chemical composition by X-Ray Photoelectron Spectroscopy (XPS), and the defective structure by Raman spectroscopy. The half-cell activity and electrochemical impedance was studied. Reliable predictions of the electrode performance could not be made by the spectroscopic results prior to electrochemistry. Therefore, we characterized the samples a second time by XPS and Raman spectroscopy after half-cell electrochemistry. The changes of the surface moieties and the stability of edge sites were monitored. They were found to differ based on the sample and the specific half-cell electrolyte used. Our results allow new conclusions for the importance and role of OFGs and their relationship to graphitic edge sites.

2. Results and Discussion

A set of four different samples with varying defect density and concentration of OFGs was prepared by refined conventional modification techniques. In the following paragraphs a pre-characterization of the samples is conducted to understand the structural and chemical changes caused by the treatment and its respective influence on the electrochemical performance thereafter. A pristine graphite felt (GF) was treated with a MWCNT in water dispersion (GF/CNT), a 4 M KOH solution (GF/KOH), and a MWCNT in 4 M KOH dispersion.

2.1. Structural and Morphological Characterization

To study the influence of the MWCNT impregnation and the KOH activation on the morphology, the felts were investigated by SEM. In Figure 1, the pristine GF (Figure 1(a–c)) consists of randomly entangled fibers with an average diameter of $\sim 9 \mu\text{m}$, possessing a smooth surface with visible stripes from the spinning process. The images of GF/CNT (Figure 1(d–e)) display no visible MWCNT aggregates in the pore space between the

fibers. Instead, a uniform coating on the surface with smaller agglomerates ($< 5 \mu\text{m}$) in between is visible. The high magnification image in Figure 1(f) demonstrates the distribution of single MWCNTs. GF/CNT has a rougher appearance than GF because of the attachment of MWCNTs and binder to the spinning pores. Different polymers have been investigated as dispersion agent and binder for the attachment of MWCNTs, of which CMC delivered the best results to obtain a homogeneous coating. UV-Vis and Dynamic Light Scattering (DLS) characterizations of various MWCNT dispersions and SEM images of impregnated felts are given in the Supporting Information (see Figure S1–S3).

The high magnification image of GF/KOH (Figure 1(i)) shows thorough roughening of the surface, especially in comparison to Figure 1(c), due to the activation process, revealing pores on the nanometer scale.^[11,30] In combination with the MWCNT impregnation, the roughening disguises the visibility of single MWCNTs because of the high edge surface contrast. However, smaller agglomerates of $\sim 3 \mu\text{m}$ as in Figure 1(k) are visible. A close comparison of GF/KOH with and without CNTs (see Figure 1(i) and 1(l)) reveals a slightly fuzzier and fluffy appearance of the MWCNT impregnated fibers indicating that the GF/CNT/KOH sample is also homogeneously decorated with MWCNTs.

We further investigated the influence on the microstructure by X-Ray Diffraction (XRD) (Figure S4). After the KOH treatment, a weak Bragg reflection is located at $2\theta \approx 31^\circ$, which is associated with residual K_2CO_3 formed during the activation treatment. While the peak width of the graphitic 002 reflection ($2\theta \approx 26^\circ$) changes only slightly (FWHM + 0.3°), the interlayer distance is expanded from 3.48 to 3.63 Å according to Bragg's law due to intercalation of metallic potassium.^[34]

2.2. Raman Spectroscopy

Raman spectroscopy was used to investigate the degree of disorder, which is introduced on the felts by the modifications. The main features of a graphite Raman spectrum (Figure 2(a)) constitute the G band at $\sim 1580 \text{ cm}^{-1}$, associated with a first order E_{2g} longitudinal optical phonon mode, resembling the in-plane stretching of C=C bonds, and the D band at $\sim 1350 \text{ cm}^{-1}$, induced by disorder such as edges, stacking fault, or atomic defects, corresponding to a A_{1g} breathing mode of a six-atom C-ring.^[35,36] The intensity ratio of the D and G band provides useful information about the degree of disorder.^[37,38] A higher ratio corresponds to a higher number of defects. As a result of the overlapping G and D' modes, the raw spectra (Figure S5) must be deconvoluted. An example of a fit to discriminate these vibrational modes is demonstrated in Figure 2(b–c). In total, 9 peaks were used to deconvolute the first- and second-order signals. The position of the D* and D'' bands is only estimated with uncertainty due to the low intensity and unclear scattering origin (see Supporting Information for details).

Figure 2(b) and 2(d–f) display the deconvoluted first-order spectra of the pristine and modified felts, showing that the initial I_D/I_G ratio of pristine GF (1.85) is increased to 2.17 by KOH

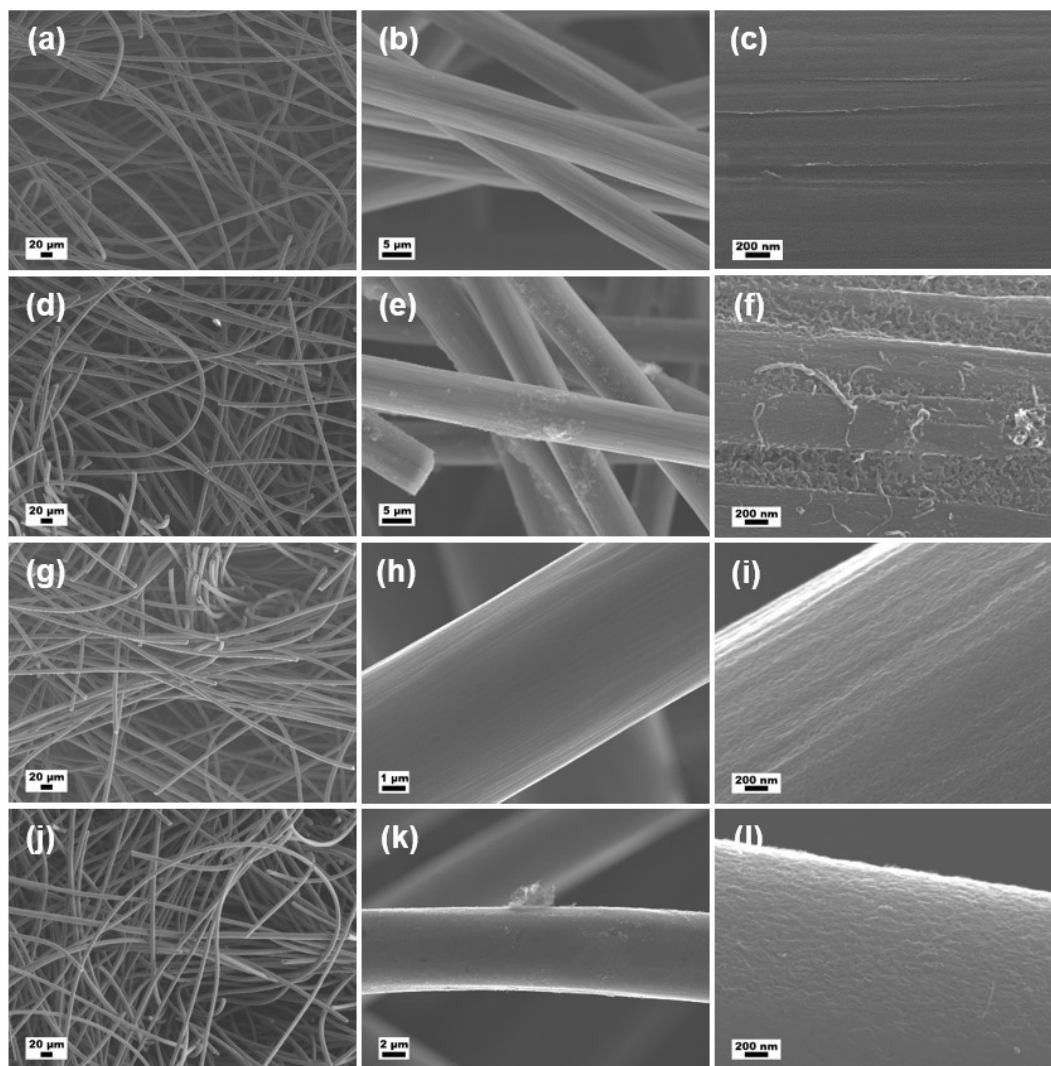


Figure 1. Scanning Electron Microscopy images at different magnifications of a–c) pristine GF, d–e) GF/CNT, g–i) GF/KOH, and j–l) combinatorial treated GF/CNT/KOH.

etching, but to an even higher extent for GF/CNT/KOH (2.33). The reduction of disorder on GF/CNT (1.57) is attributed to the high graphitic character of single MWCNTs attached to the fiber, and probably their preferred attachment to fiber defect sites (such as in the spinning stripes in Figure 1(f)). The highly defective structure of GF/CNT/KOH is associated with additional defects created on the MWCNT surface by KOH, and the different interaction characteristics between the basal plane of GF, and the nanostructured surface of GF/KOH with MWCNTs. The second assumption is based on the analysis of the second-order modes (Figure 2(g)), where a more intense 2D band for GF/CNT indicates strong interaction between single-atom graphitic layers.^[39] The aggressive attack on the graphitic structure induced by KOH is also visible in a decreased 2D band for GF/KOH and GF/CNT/KOH. As it is seen by SEM (see Figure 1(i)), the KOH activation creates a nanostructured surface, thus providing access to underlying edge site oriented planes, and introducing defects into the basal plane on the outer surface of the felt.

In summary, by Raman spectroscopy analysis we observed an overall decrease of disorder by the coating with MWCNTs, an increase after KOH activation, and an even higher number of defects by combining the MWCNT attachment with the KOH treatment. The origin of the observed defects is evaluated by the ratio of the D and the D' band, in which a ratio of ~ 3.5 corresponds to grain boundary defects such as edge sites, and higher ratios to vacancy-like (~ 7) or sp^3 type (~ 13) defects.^[40] The ratios of our samples are between 2.56 (GF/CNT) and 2.91 (GF/CNT/KOH), which is why we characterize the defects on our samples as edge site like. Due to a ratio < 3.5 , we have multiple edge sites in a so-called loop configuration.^[41]

2.3. X-Ray Photoelectron Spectroscopy

The surface chemical composition has been studied by XPS to compare the OFGs qualitatively and quantitatively. Prior to a detailed investigation, a survey spectrum is recorded to check

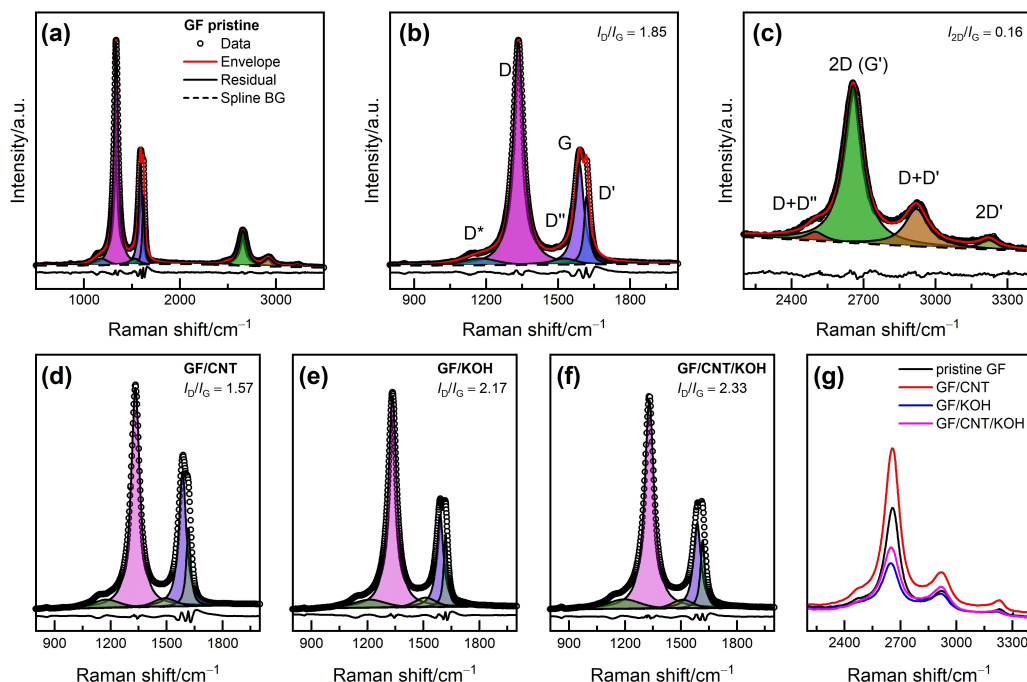


Figure 2. Deconvoluted Raman spectra of all graphite felt samples. Top row: analysis of pristine GF, displaying a) the survey spectrum with the used spline background and more detailed regions representing b) the first-order and c) the second-order modes. Bottom row: detail spectra of d) GF/CNT, e) GF/KOH, f) GF/CNT/KOH, and g) the overtones of all samples in comparison. All spectra were normalized to the D band and deconvoluted by absolute Lorentzian and Gaussian-Lorentzian shape functions. The given I_D/I_G ratio is the average of at least three measurements per sample.

for sample contamination (Figure S6). Detail spectra were taken from the core level regions O 1s and C 1s (Figure 3). Three main

oxygen species were identified on every sample: O–C (hydroxyl groups) at binding energies of ~ 532.8 eV, O=C (carbonyl groups) at ~ 531.6 eV, and O=C–OH (carboxyl groups) at 533.9 eV.^[42] Adsorbed water is present on all felts above 535 eV. The water content increases after KOH activation from below 0.2 to ~ 0.5 at%, suggesting improved wetting properties.^[11] After the KOH treatment, residual carbonate groups are present at 530.6 eV and ~ 292.9 eV.

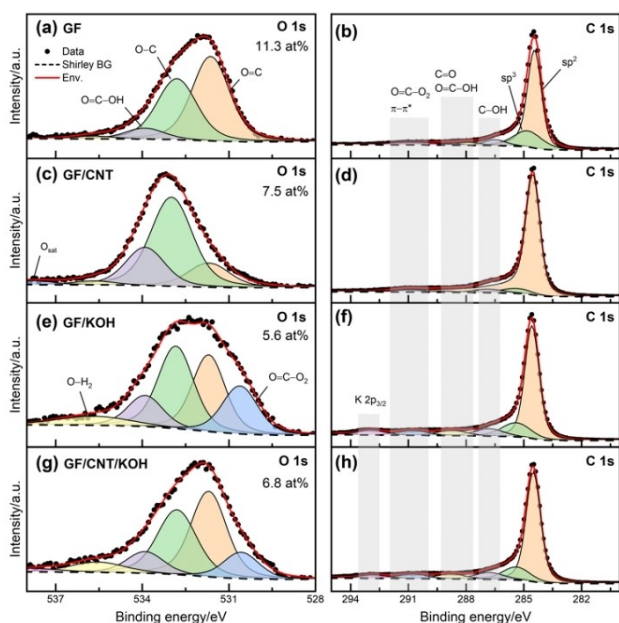


Figure 3. Deconvoluted X-Ray photoelectron detail spectra of the oxygen core level O 1s and carbon core level C 1s. From top to bottom: a–b) pristine GF, c–d) GF/CNT, e–f) GF/KOH, and g–h) GF/CNT/KOH are displayed. The regions were subtracted by a Shirley background and single species fitted by Gaussian-Lorentzian peak shapes. The concentration of surface oxygen for the sample is given.

We evaluated the concentration of oxygen in comparison to the total carbon–oxygen content and the share in one specific oxygen group within the three OFGs (Table S1). By the application of MWCNTs to GF (~ 11 at%), the overall oxygen content is reduced to ~ 8 at%, and a higher amount of sp^2 hybridized carbon (~ 81 at%) is present (Figure 3(d)). After KOH etching, the oxygen concentration is further reduced to ~ 6 at% (GF/KOH) and ~ 7 at% (GF/CNT/KOH). This is surprising, since the Raman spectroscopy and SEM results suggested more edge sites, which are expected to possess bonds to oxygen atoms. According to the C 1s region, the relative amount of sp^2 hybridized carbon is even increased from ~ 57 at% (GF) to about 60–62 at%. This can be explained by the exposure of underlying graphite sheets due to the etching treatments, which reveal a lower oxygen coverage than the surface layers of pristine GF.

The C 1s region exhibits five different carbon components, related to sp^2 and sp^3 hybridized carbon at ~ 284.5 eV and ~ 285.2 eV, along with hydroxyl, and carbonyl/carboxylic groups at ~ 286.6 eV and ~ 287.8 eV.^[15,43] We did not discriminate between carbonyl and carboxyl groups, since the assignment of

binding energies for the respective species is ambiguous in literature.^[44–48] The discrimination is further impeded by the relative low intensity of the single oxygenated carbon species (< 5 at%) compared to the signal of sp^2 carbon (> 57 at%). At higher binding energies of 289.0–291.7 eV it was close to impossible to distinguish between carbonates, adsorbed atmospheric carbon components, and the shake-up satellite feature associated with graphitic carbon, all present at about 291 eV.^[42,44]

2.4. Electrical Conductivity

The influence of the felt modifications on the electrical properties has been evaluated by performing pressure dependent conductivity measurements. To guarantee homogeneous potential distribution for a felt electrode, the fiber conductivity, which relies heavily on the fiber–fiber interface, should be high.^[49,50] The compression inside a battery minimizes ohmic losses, while the permeability of flowing electrolyte through the pores should be maintained.^[51] The felts reveal an initial resistivity drop (Figure 4), which is associated with the creation of interfacial contact between the fibers and the measurement device. Subsequently, the mere electrical property of the felt material is observed.^[52–54] GF shows a severe resistivity decrease when compressed by 15% of the total thickness, followed by a slight decrease thereafter to $22 \text{ m}\Omega \text{ cm}^2$. The MWCNTs decrease not only the contact resistance of GF/CNT ($22 \text{ m}\Omega \text{ cm}^2$ at ~8% total compression), but also increase the intrinsic conductivity ($13 \text{ m}\Omega \text{ cm}^2$ at ~21% total compression). We expect the nanostructured surface of GF/KOH to create more contact points between the fiber and the measurement device, which reduces the interfacial contribution to the resistance. For GF/CNT/KOH, the resistivity at ~20% compression is decreased from 19 (GF/KOH) to $16 \text{ m}\Omega \text{ cm}^2$. However, with respect to the deviation of GF/CNT/KOH, the MWCNTs cannot enhance the electrical conductivity of the felt electrode completely homogeneously

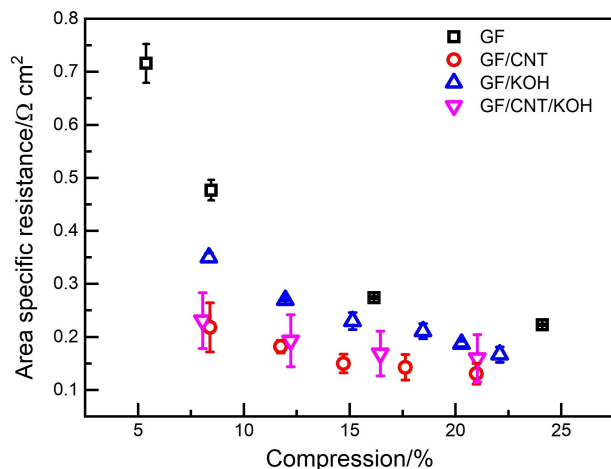


Figure 4. Measurement of the electrical area specific resistance under a given felt compression of pristine and modified graphite felts.

due to the lower mechanical stability in the investigated region (Figure S7).

2.5. Electrochemical Characterization

To study the influence of the sample modifications, which created edge sites and OFGs in various concentrations, electrochemical half-cell tests were performed. The electrocatalytic properties were investigated by cyclic voltammetry (CV). In each obtained voltammogram, the peak separation potential (ΔE_p) and the peak current ratio from the oxidation and reduction peaks are used to study the activity and the redox reversibility. For the positive half-cell (Figure 5(a)), a reduction of ΔE_p from GF (290 mV) to GF/CNT (150 mV) is observed (see Supporting Information and Figure S8 for details on the performance regarding the sample preparation), which is according to the XPS, Raman spectroscopy, and resistivity results a consequence of the higher electrical conductivity of the felt electrode. For catalytically more active samples, a sharp oxidation signal at 0.7 V vs. Ag/AgCl and a broad reduction at 0.2–0.6 V vs. Ag/AgCl corresponds to the $V^{IV}O^{2+}/V^{III}$ redox reaction (compare Figure S9). The electrochemical performance of GF/KOH depends on the molarity of the KOH solution, the drying procedure, and subsequent heating temperature (Figure S10), and has an optimized ΔE_p of 70 mV.^[11,30,55] No further electrocatalytic improvement is observed by combining the KOH activation and the impregnation with MWCNTs. Compared to the XPS and Raman results, the best performing samples showed a low degree of oxygenation and an increased number

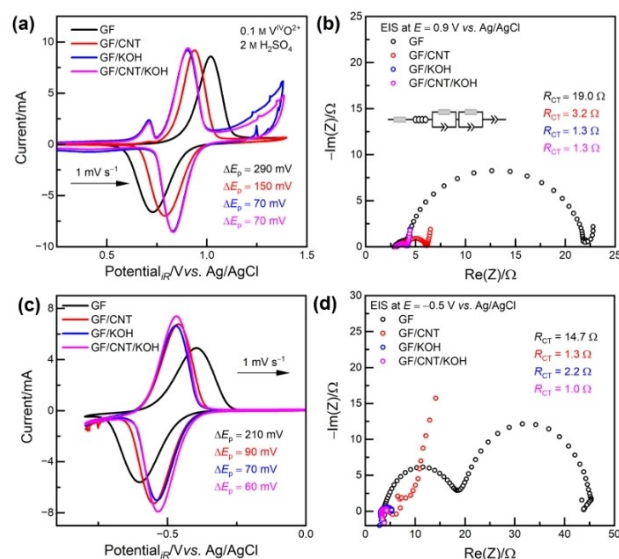


Figure 5. Electrochemical characterization of the pristine and the modified graphite felt electrodes in both half-cells, measured in a three-electrode cell. a) iR corrected cyclic voltammetry with 1 mV s^{-1} for the positive half-cell; b) electrochemical impedance spectra at 0.9 V vs. Ag/AgCl, also displaying the equivalent circuit diagram used for spectra deconvolution (see Experimental Section for details); c) iR corrected cyclic voltammetry with 1 mV s^{-1} for the negative half-cell; d) electrochemical impedance spectra at -0.5 V vs. Ag/AgCl.

of edge sites. The superior electrocatalytic activity of edge sites compared to basal plane graphite has been studied in literature and is shown in Figure S11 by performing CV on pyrolytic graphite electrodes.^[17,18]

We additionally evaluated the charge-transfer resistance (R_{CT}) by electrochemical impedance spectroscopy (EIS) at an applied potential. In the Nyquist representation (Figure 5(b)), the main semicircle corresponds to R_{CT} , which is significantly decreased from 19.0 Ω (GF) over 3.2 Ω (GF/CNT) to 1.3 Ω (GF/KOH and GF/CNT/KOH) due to the felt modifications. R_{CT} is reduced by all modifications, but to the highest extent for those samples that revealed a lot of edge sites and a lower oxygen concentration. The MWCNTs provide good charge-transfer, which we assume is related to the high electrical conductivity and low interfacial resistance, since we observed less edge sites for this sample.

The mass-transfer properties of the electrodes are studied by the Randles–Sevcik equation (Figure S12 and S13). A linear fit suggests that the $V^{VO_2^+}/V^{VO^{2+}}$ redox reaction is limited by diffusion.^[27,56] The reductive fit reveals a $\sim 70\%$ higher slope for the KOH activated samples, signifying faster reaction kinetics at the electrode.^[48] This shows a positive influence of edge sites for the kinetics and indicates a hindering effect of oxygen for the $V^{VO_2^+}/V^{VO^{2+}}$ reduction.^[21]

Based on the electrochemical analysis of the positive half-cell, we conclude that the activity of the pristine GF is enhanced both by the MWCNT application and KOH activation. There was almost no difference observed between the KOH treatment of the felt only and both felt and MWCNTs in combination. For these two samples, it seems that neither the relative amount of one specific OFG (O–C on GF/KOH and O=C on GF/CNT/KOH), nor the difference in defect density (2.17 and 2.33) has a major impact on the activity of the $V^{VO_2^+}/V^{VO^{2+}}$ redox reaction. If one considers carboxylic groups to drive the positive half-cell redox reaction, GF/CNT would be expected to outperform the other samples, which was clearly not the case.

The negative half-cell reaction was also inspected by the same electrochemical techniques. The CV curves in Figure 5(c) display an improvement of the redox activity, reducing the peak potential separation in the order GF ($\Delta E_p = 210$ mV) > GF/CNT ($\Delta E_p = 90$ mV) > GF/KOH ($\Delta E_p = 70$) > GF/CNT/KOH ($\Delta E_p = 60$ mV). This proves that all modifications also have a positive effect on the electrocatalytic activity for the V^{III}/V^{II} redox reaction. In the Nyquist plots (Figure 5(d)), R_{CT} decreases from 14.7 Ω (GF) to 2.2 Ω (GF/KOH), 1.3 Ω (GF/CNT), and 1.0 Ω (GF/CNT/KOH). At lower frequencies, a second semicircle is visible for GF, which is assigned to a $V^{VO^{2+}}/V^{III}$ reduction process of residual higher oxidized vanadium species. Given by the linear fit of the Randles–Sevcik plots (Figure S13), the slope of GF/CNT/KOH is $\sim 65\%$ higher for both anodic and cathodic currents, indicating a faster mass transfer in the combinatorial treated electrode.

In summary, the combination of KOH etching and MWCNT impregnation has a positive effect compared to only one of the methods, which one might therefore ascribe to either the higher (or lower) concentration of one specific OFG, or the additional edge sites on the electrode which are beneficial for

the charge-transfer and the electrocatalytic activity, since the defect-poor GF/CNT with the higher oxygen concentration reveals the lowest improvement.

In addition to the half-cell characterization, the electrochemical active surface area has been investigated in a non-faradaic potential region (Figure 6(a)) to probe the electrochemical double layer capacitance (EDLC). A relatively low EDLC of 1.9 mF is revealed for GF, which is significantly enhanced by a factor of ~ 33 for GF/CNT/KOH (63.2 mF). The increase is attributed to the enhancement of the overall surface area by etching a microporous structure on GF and by attaching high surface MWCNTs, which can provide additional active sites. Further, more edge sites are introduced to the graphitic structure of the electrode as well as on the MWCNTs, which relates to the higher EDLC of edge planes (~ 70 $\mu\text{F cm}^{-2}$) compared to basal planes ($1\text{--}2$ $\mu\text{F cm}^{-2}$) of graphite.^[11,57,58] For this reason it is surprising that the EDLC of GF/KOH is even higher (73.7 mF), though it revealed a lower number of defects in Raman spectroscopy. Further studies towards the phenomena of the EDLC, its relation to the active surface area, and the influencing factors are intended. Our XPS results already imply that the initial relative amount of oxygen does not play the major role, when the active surface area is investigated.

2.6. Evolution of Oxygen Functional Groups and Graphitic Defects in Electrochemistry

By the comparison of the electrochemical results with the previous physicochemical analysis, the initial concentration of oxygen did not sufficiently explain the differences in half-cell performance. If we consider ΔE_p , R_{CT} , mass-transfer, and the reversibility of the redox reaction, the activity for the positive half-cell is in the order GF/CNT/KOH = GF/KOH > GF/CNT > GF, and similar in the negative half-cell, with GF/CNT/KOH exceeding the performance of GF/KOH. Based on the initial XPS analysis and the role of OFGs (Table S1), as it is described in literature, one would expect activities for the positive half-cell in the order GF/CNT > GF > GF/CNT/KOH > GF/KOH, considering the overall concentration of carboxylic groups. For hydroxyls as active species it would be GF > GF/CNT > GF/KOH > GF/CNT/KOH. However, none of these sequences is reflected in electro-

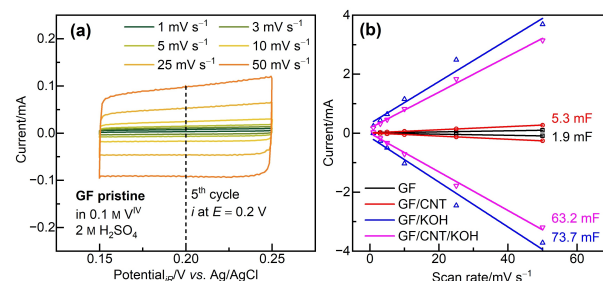


Figure 6. Electrochemical double layer capacitance of pristine and modified graphite felt electrodes; a) cyclic voltammetry in a potential range without the observation of faradaic processes at different scan rates, b) plot of current at a potential of 0.2 V vs. Ag/AgCl for each given scan rate.

chemistry. Also, by considering the relative stoichiometry of OFGs compared to each other, it is not possible to reflect the above-mentioned sequences. On the contrary, an increase of surface groups rather seems to have a negative impact on the electrocatalytic activity. To better understand the influence of the electrochemical conditions on the OFGs, their evolution was studied by XPS after cycling. The deconvoluted O 1s and C 1s detail spectra of all samples are displayed in Figure 7(a–d) and Figure S14. For deconvolution of the detail spectra, the same restrictions as for the samples in the initial state applied, allowing binding energy and FWHM shifts of ± 0.2 eV.

After cycling in the positive half-cell, the relative oxygen content increases from ~6–11 at% for the initial samples by around a factor of 3 for the cycled electrodes. This effect is most pronounced for GF/CNT, which reveals an oxygen content of more than 35 at%. Besides GF/CNT, the other samples have a very similar quantity of surface oxygen (~20–24 at%). Therefore, the oxygen concentration alone cannot explain the different electrochemical activities, which fuels the question about the role of different OFGs. To study the influence of single OFGs,

their evolution has been analyzed quantitatively, comparing the relative percentage values of O–C, O=C, and O=C–OH in the initial state and after electrochemistry (Figure 7(e–g)).

On the one hand, GF/CNT reveals the lowest relative number of hydroxyls after cycling (28%). On the other hand, the highest concentration of hydroxyls after electrochemistry is present on GF (60%), which had the lowest half-cell performance. Both GF/KOH and GF/CNT/KOH, which showed an equally high electrochemical performance, have values in between. The influence of carboxylic groups is not obvious at first sight, too. Most of the oxygen on GF/CNT consists of carbonyl (~69%) and only ~3% of carboxylic groups. GF/KOH and GF/CNT/KOH developed lower amounts of carbonyls (52% and 45%) with more persistent carboxylic groups (8% and 11%). It is seen that the relative concentration on GF/KOH undergoes some severe changes during cycling (especially for C=O and O=C–OH groups), while GF/CNT/KOH has a similar share in OFGs compared to the initial sample.

One might argue that the higher activity of GF/CNT compared to GF (~6% carboxylic groups) is attributed to the

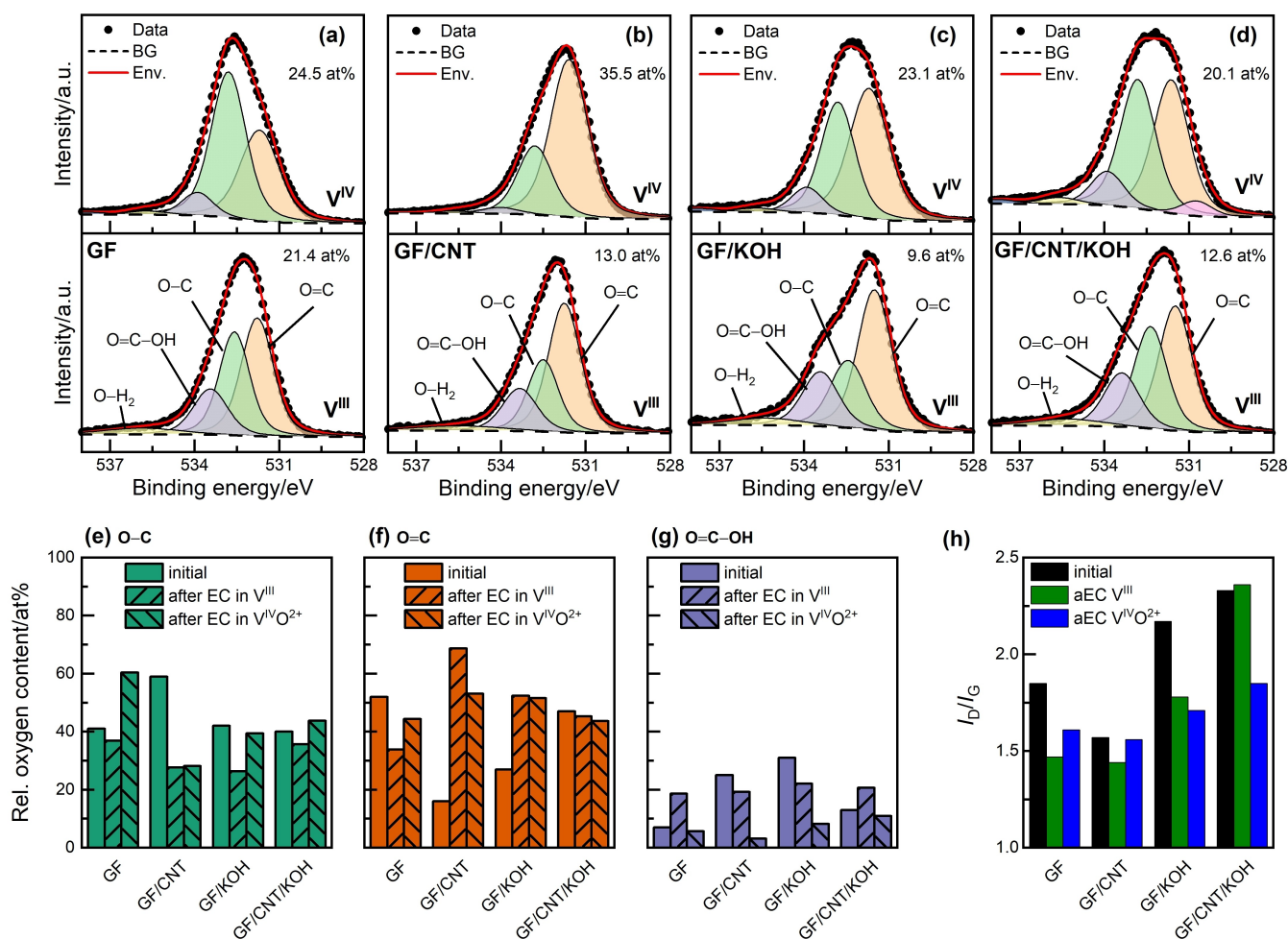


Figure 7. Analysis of the pristine and modified graphite felt electrodes after cycling regarding their surface functional group composition and defective structure. X-Ray photoelectron detail spectra of a) GF, b) GF/CNT, c) GF/KOH, d) GF/CNT/KOH, displaying the O 1s core level region. Comparison of the relative number of oxygen functional groups, namely e) hydroxyl f) carbonyl and g) carboxylic groups; h) the defect structure was studied by Raman spectroscopy, evaluating the I_b/I_g ratios before and after cycling in each half-cell.

severe reduction of electrical resistance, which compensates the lower amount of active carboxylic groups. However, this is expected to mainly influence the charge-transfer resistance, but also an impact on the electrocatalytic activity and the active surface area was observed.

Since the XPS results were not in itself conclusive, the degree of disorder after electrochemistry has been investigated by Raman spectroscopy (Figure S15). The stability of edge sites is important, since OFGs on edge plane graphite are far more stable than on basal planes.^[20] In Figure 7(h), the I_D/I_G ratios are given for each sample before and after cycling in the corresponding half-cell. After cycling in the positive half-cell, all samples lose a severe number of edge sites, reflected by a decrease of the I_D/I_G ratio. Considering the degree of disorder, we attribute the minor electrochemical performance of GF mostly to its lower number of defects ($I_D/I_G = 1.61$). More stable carboxylic groups are formed on GF/KOH and GF/CNT/KOH, which correlates with their higher defect density ($I_D/I_G = 1.71$ and 1.85). The higher defect density is therefore an account for the higher activity of these samples for the positive half-cell reaction.

The minor differences in the chemical composition regarding the number of carboxylic groups is not expected to drive such high discrepancies in the electrochemical performance. It is much rather a consequence of their primary formation on edge sites if the correlation to the overall degree of disorder is considered. Due to the decrease of edge sites during oxidative treatment in the positive half-cell, we suppose that other oxygen groups, as the concentration of carboxylic groups also decreases (Figure 7(g)) are attached to active edge sites and hinder the electron transfer subsequently.

The negative half-cell was analyzed in the same manner. Cycling in V^{III} introduces fewer oxygen moieties (~10–13 at%) for the modified felts, while the pristine GF had a considerably larger oxygen content of >20 at%. This observation suggests, that, also for the negative half-cell, the relative amount of oxygen is a property that describes the activity of the graphite felt electrodes poorly. Therefore, the composition of single OFGs has been evaluated, showing that the surface composition of all felts is relatively similar, with about 19–22% carboxylic, 44–53% carbonyl, and 26–37% hydroxyl groups. Again, no clear correlation between the relative concentration of a certain OFG and the electrochemical activity of the electrodes could be established. A possible explanation for this observation might be that the activity of certain OFGs for the V^{III}/V^{II} redox reaction seems to depend on whether they are attached to basal or edge site positions and a higher catalytic activity was attributed to oxygen containing edge site defects.^[18,19,62] Hence, it is important to further investigate the change in disorder after electrochemistry. The I_D/I_G ratio is affected by cycling, which leads to a decrease of defects on GF (1.47), GF/CNT (1.44), and GF/KOH (1.78) while the amount of edge sites is increased on GF/CNT/KOH (2.36). Based on these observations, our investigation seems to be consistent with the previously discussed studies about the importance of edges. Due to the minor differences in the surface chemical composition observed by XPS, we conclude that graphitic edge sites

appear to be the major driving force for the negative half-cell reaction. Nevertheless, OFGs form on the surface of graphite felt electrodes during electrochemical cycling. But a positive influence of these OFGs on the negative half-cell reaction cannot be confirmed by our study. Instead, the evolution of defect density on the surface appears to be a more important indicator for the electrocatalytic activity.

3. Conclusions

The role of graphitic edge sites and OFGs, and their electrochemical stability in both half-cells of a VFB was examined. Our chosen graphite felt electrode treatments resulted in samples with a different concentration of oxygen moieties and disorder. The disorder was characterized as edge site defects for all samples. By XPS and Raman spectroscopy after half-cell tests, we confirmed that the OFGs and edge sites dynamically evolve during cycling. Therefore, the electrochemical performance of an electrode cannot only be correlated with its physicochemical properties in the pristine state. Neither the concentration of OFGs nor the presence of a certain type of OFG could be made responsible for the electrocatalytic activity of the electrodes. Instead, the more active ones revealed a lower oxygen concentration and simultaneously a higher number of edge sites. We observed a correlation between the electrochemical performance and the electrochemical stability of edges and attribute this as beneficial towards the $V^{IV}O_2^+/V^{III}O_2^+$ and the V^{III}/V^{II} redox reactions. Our study highlights the importance of edge site defects for the vanadium redox kinetics for both the positive and negative half-cell reaction. Though we cannot rule out that certain OFGs are active during the reaction, edge site defects seem to play an essential role either by stabilizing favorable OFGs or by directly assisting the charge-transfer process.

Experimental Section

Sample preparation

Sheets of polyacrylonitrile based graphite felt (GFD 4.6, SGL Carbon) were cut out and cleaned by sonication in acetone and ultrapure water ($18.2 \text{ M}\Omega \text{ cm}^{-1}$) for 10 min each, followed by drying at 80°C overnight. Multi-walled carbon nanotube (MWCNT) dispersions were facilitated by dissolving 1 mg mL^{-1} CMC in ultrapure water and adding 2 mg mL^{-1} MWCNT (Baytubes, BAYER) in a 180 min sonication process. Alkaline etching solutions were prepared by dissolving KOH (Emplura) in ultrapure water. For a combined process, the MWCNT dispersion was mixed with 8 M KOH in equal parts. To prepare the desired sample, pieces of GFD 4.6 were immersed in the different solution or dispersion, followed by a vacuum treatment to ensure thorough wetting. A freeze-drying step was incorporated to improve the distribution of MWCNTs and the KOH activating agent on the felt.^[63,64] The wet samples were transferred to a freeze-dryer (LyoQuest –85, Telstar), frozen at -85°C for 24 h, followed by drying for at least 48 h. The dry samples were heated in a batch type furnace in argon atmosphere, by ramping with 3 K min^{-1} to 800°C for 1 h. Afterwards, the samples were cleaned with diluted H_2SO_4 and ultrapure water and

dried again over night at 80 °C. The pristine felt is denoted as GF, and the other felts with respect to their prior treatment GF/CNT (treated with MWCNT dispersion), GF/KOH (treated with 4 M KOH), and GF/CNT/KOH (treated with MWCNT dispersion in 4 M KOH).

Structural and physicochemical characterization

The MWCNT dispersions were diluted with ultrapure water and characterized with UV-Vis spectroscopy (Hitachi U-3010 Spectrophotometer) in a range of 900–190 nm using quartz cuvettes (Hellma 100-QS), and Dynamic Light Scattering (Zetasizer Pro, Malvern Panalytical). The felt morphologies were investigated by Scanning Electron Microscopy (MERLIN, Carl Zeiss) with an acceleration voltage of 10–15 kV and a probe current of 150–500 pA. Raman spectra were recorded with a LabRAM HR Evolution spectrometer (HORIBA Scientific), using a HeNe laser with a wavelength of 632.8 nm ($E_{\text{laser}} = 1.9876$ eV), further using a 600 gmm^{-1} grating and a 100 \times magnification objective. At least three spectra were taken on every sample to check the variance of the results. All spectra were normalized to the highest signal, subtracted by a spline background, and fitted by Lorentzian and Gaussian-Lorentzian (D^* and D') peak shapes. X-Ray Photoelectron Spectroscopy was performed using a K-alpha⁺ spectrometer (Thermo Fischer Scientific) with monochromatic Al-K α_1 radiation ($\lambda = 1486.6$ eV), with a spot size of ~ 400 μm . Survey spectra were recorded with a pass energy of 200 eV, detail spectra with 50 eV. The Thermo Avantage software was used for data acquisition and spectra deconvolution, determining a Shirley background with the implemented smart background function. The asymmetry of sp^2 hybridized graphitic carbon was evaluated with a tail mix of 50–90% and a tail exponent of 0.03–0.1, considering a smaller FWHM of 0.8–0.9 eV. All other components were fitted using conventional Gaussian-Lorentzian peak profiles with FWHM values of 1.5–1.8 eV, restricting the position with respect to the sp^2 signal and the relative FWHM to the sp^3 hybridized carbon. The concentration of oxygen was analyzed by quantifying all O 1s and C 1s components present on the surface of a sample. Further, we quantified the concentration of each specific oxygen group, and the ratio of the three main oxygen functional groups to each other. The X-Ray Diffraction patterns were measured with a STOE STADI P powder diffractometer using monochromatic Cu-K α_1 radiation ($\lambda = 1.54056$ Å) in transmission geometry. For the investigation of the electrical conductivity under compression, a uniaxial compression device (zwickLine, Zwick/Roell) with a 100 N load cell was used. The thickness at no compression of the graphite felts was calculated by the distance of the compression tools at 0.1 N. By knowing the thickness at a given force, the compression is derived. The test machine was coupled with a custom-built cell to measure the electrical conductivity. Gold coated copper pins connected to a potentiostat (BioLogic SP-300) are attached to the load cell; insulating plates made from yttrium stabilized zirconium oxide prevent short circuiting through the compression device. The voltage was measured at a current of 100 mA, and the area specific resistance was calculated by $\rho_{\text{el}} = R \times A$, with R being the electrical resistance and A the felt contact area. To receive a standard deviation (error bars in Figure 4), three samples were tested for each modification.

Electrochemical characterization

Cyclic voltammetry and electrochemical impedance spectroscopy were measured with a BioLogic SP-300 potentiostat, using a custom-built three electrode cell. Graphite felt in contact with a gold coated copper disk, bridged by a glassy carbon plate was used as working, a pristine graphite felt connected to a glassy carbon

rod as counter, and Ag/AgCl in 3 M KCl ($E_{\text{Ag/AgCl}} = 0.210$ V vs. RHE) as reference electrode. Prior to the measurement, the felt was immersed in the corresponding electrolyte under vacuum to ensure thorough wetting. As electrolyte, 0.1 M $\text{V}^{\text{IV}}\text{O}^{2+}$ in 2 M H_2SO_4 was prepared from VOSO_4 (Alfa Aesar) and concentrated H_2SO_4 (Emsure). The electrolyte was bubbled with argon prior to, and during the experiment above the electrolyte. For the negative half-cell, the electrolyte was discharged in a full cell to receive 0.1 mV^{III}. The data was corrected regarding the electrolytic resistance (3 to 3.5 Ω) with impedance spectroscopy. Impedance spectra were further recorded with a voltage amplitude of 10 mV at an applied potential of 0.9 V and -0.5 V vs. Ag/AgCl. Fitting of the spectra was done with RelaxIS 3 (rhd instruments). The equivalent circuit diagram therein consists of $R_{\text{el}}-L-(RQ_{\text{GF}})-(RQ_{\text{CT}})-Q_{\text{diff}}$, with L corresponding to an inductance, R_{el} to the resistance of the electrolyte, RQ_{GF} and RQ_{CT} to a resistance (R) and a constant phase element (Q) of the electrode/current collector and electrode/electrolyte (charge-transfer) interfaces in parallel. Q_{diff} resembles the diffusion element, which describes the mass transport of the electrolyte to the graphite felt surface. The electrochemical double layer capacitance was measured in a potential window of 0.15–0.25 V vs. Ag/AgCl, with a method that is in detail described elsewhere.^[65] Briefly, the potential was kept at 0.2 V vs. Ag/AgCl for 2 min before scanning the potential region with a given scan rate. Considering the anodic and cathodic current at 0.2 vs. Ag/AgCl in the 5th cycle, the slope of a current vs. scan rate plot reveals the capacitance.

Acknowledgements

The financial support by the German Federal Ministry of Education and Research within the project Flow3DKat (03EK3053 C) is gratefully acknowledged. The authors thank Tianzhu Liu for assistance with the DLS measurement, and the AK Bensch at Kiel University for providing the multi-walled carbon nanotubes. Open access funding enabled and organized by Projekt DEAL.

Conflict of Interest

The authors declare no conflict of interest.

Keywords: vanadium flow battery · oxygen functional groups · graphite felt electrodes · graphitic defects · carbon nanotubes

- [1] H. R. Byon, B. M. Gallant, S. W. Lee, Y. Shao-Horn, *Adv. Funct. Mater.* **2013**, *23*, 1037.
- [2] Y. Huang, L. Sun, Z. Yu, R. Jiang, J. Huang, Y. Hou, F. Yang, B. Zhang, R. Zhang, Y. Zhang, *Catal. Sci. Technol.* **2020**, *10*, 2627.
- [3] H. Cao, X. Peng, M. Zhao, P. Liu, B. Xu, J. Guo, *RSC Adv.* **2018**, *8*, 2858.
- [4] B. Sun, M. Skyllas-Kazacos, *Electrochim. Acta* **1992**, *37*, 2459.
- [5] W. Li, J. Liu, C. Yan, *Carbon* **2013**, *55*, 313.
- [6] S. Zhong, C. Padeste, M. Kazacos, M. Skyllas-Kazacos, *J. Power Sources* **1993**, *45*, 29.
- [7] Y. Li, J. Parrondo, S. Sankarasubramanian, V. Ramani, *J. Phys. Chem. C* **2019**, *123*, 6370.
- [8] A. M. Pezeshki, J. T. Clement, G. M. Veith, T. A. Zawodzinski, M. M. Mench, *J. Power Sources* **2015**, *294*, 333.
- [9] W. Zhang, J. Xi, Z. Li, H. Zhou, Le Liu, Z. Wu, X. Qiu, *Electrochim. Acta* **2013**, *89*, 429.
- [10] L. Yue, W. Li, F. Sun, L. Zhao, L. Xing, *Carbon* **2010**, *48*, 3079.
- [11] Z. Zhang, J. Xi, H. Zhou, X. Qiu, *Electrochim. Acta* **2016**, *218*, 15.

- [12] Z. He, Y. Jiang, W. Meng, F. Jiang, H. Zhou, Y. Li, J. Zhu, L. Wang, L. Dai, *Appl. Surf. Sci.* **2017**, *423*, 111.
- [13] K. J. Kim, S.-W. Lee, T. Yim, J.-G. Kim, J. W. Choi, J. H. Kim, M.-S. Park, Y.-J. Kim, *Sci. Rep.* **2014**, *4*, 6906.
- [14] K. J. Kim, Y.-J. Kim, J.-H. Kim, M.-S. Park, *Mater. Chem. Phys.* **2011**, *131*, 547.
- [15] L. Estevez, D. Reed, Z. Nie, A. M. Schwarz, M. I. Nandasiri, J. P. Kizewski, W. Wang, E. Thomsen, J. Liu, J.-G. Zhang, V. Sprenkle, B. Li, *ChemSusChem* **2016**, *9*, 1455.
- [16] J. Maruyama, T. Hasegawa, S. Iwasaki, T. Fukuhara, M. Nogami, *J. Electrochem. Soc.* **2013**, *160*, A1293-A1298.
- [17] G. Zhang, A. S. Cuharuc, A. G. Güell, P. R. Unwin, *Phys. Chem. Chem. Phys.* **2015**, *17*, 11827.
- [18] N. Pour, D. G. Kwabi, T. Carney, R. M. Darling, M. L. Perry, Y. Shao-Horn, *J. Phys. Chem. C* **2015**, *119*, 5311.
- [19] M. Park, I.-Y. Jeon, J. Ryu, J.-B. Baek, J. Cho, *Adv. Energy Mater.* **2015**, *5*, 1401550.
- [20] S. M. Taylor, A. Pătru, D. Perego, E. Fabbri, T. J. Schmidt, *ACS Appl. Energy Mater.* **2018**, *1*, 1166.
- [21] H. Fink, J. Friedl, U. Stimming, *J. Phys. Chem. C* **2016**, *120*, 15893.
- [22] J. Friedl, C. M. Bauer, A. Rinaldi, U. Stimming, *Carbon* **2013**, *63*, 228.
- [23] Z. González, P. Álvarez, C. Blanco, S. Vega-Díaz, F. Tristán-López, L. P. Rajukumar, R. Cruz-Silva, A. L. Elías, M. Terrones, R. Menéndez, *Sustain. Energy Technol. Assess.* **2015**, *9*, 105.
- [24] W. Li, J. Liu, C. Yan, *Electrochim. Acta* **2012**, *79*, 102.
- [25] L. Dai, Y. Jiang, W. Meng, H. Zhou, L. Wang, Z. He, *Appl. Surf. Sci.* **2017**, *401*, 106.
- [26] Z. He, G. Cheng, Y. Jiang, L. Wang, L. Dai, *J. Electrochem. Soc.* **2018**, *165*, A932-A938.
- [27] R.-H. Huang, C.-H. Sun, T.-M. Tseng, W.-K. Chao, K.-L. Hsueh, F.-S. Shieu, *J. Electrochem. Soc.* **2012**, *159*, A1579-A1586.
- [28] D.-S. Yang, J. Y. Lee, S.-W. Jo, S. J. Yoon, T.-H. Kim, Y. T. Hong, *Int. J. Hydrog. Energy* **2018**, *43*, 1516.
- [29] C. Noh, S. Moon, Y. Chung, Y. Kwon, *J. Mater. Chem. A* **2017**, *5*, 21334.
- [30] Y. Wang, Y. Liu, K. Wang, S. Song, P. Tsiakaras, H. Liu, *Appl. Catal. B* **2015**, *165*, 360.
- [31] Z. Q. Li, C. J. Lu, Z. P. Xia, Y. Zhou, Z. Luo, *Carbon* **2007**, *45*, 1686.
- [32] B. M. Gatehouse, D. J. Lloyd, *J. Chem. Soc., Dalton Trans.* **1973**.
- [33] J. Wang, S. Kaskel, *J. Mater. Chem.* **2012**, *22*, 23710.
- [34] J. Romanos, M. Beckner, T. Rash, L. Firlje, B. Kuchta, P. Yu, G. Suppes, C. Wexler, P. Pfeifer, *Nanotechnology* **2012**, *23*, 15401.
- [35] M. S. Dresselhaus, A. Jorio, R. Saito, *Annu. Rev. Condens. Matter Phys.* **2010**, *1*, 89.
- [36] L. G. Cançado, A. Jorio, E. H. M. Ferreira, F. Stavale, C. A. Achete, R. B. Capaz, M. V. O. Moutinho, A. Lombardo, T. S. Kulmala, A. C. Ferrari, *Nano Lett.* **2011**, *11*, 3190.
- [37] F. Tuinstra, J. L. Koenig, *J. Chem. Phys.* **1970**, *53*, 1126.
- [38] D. S. Knight, W. B. White, *J. Mater. Res.* **1989**, *4*, 385.
- [39] M. A. Pimenta, G. Dresselhaus, M. S. Dresselhaus, L. G. Cançado, A. Jorio, R. Saito, *Phys. Chem. Chem. Phys.* **2007**, *9*, 1276.
- [40] A. Eckmann, A. Felten, A. Mishchenko, L. Britnell, R. Krupke, K. S. Novoselov, C. Casiraghi, *Nano Lett.* **2012**, *12*, 3925.
- [41] P. Puech, M. Kandara, G. Paredes, L. Moulin, E. Weiss-Hortala, A. Kundu, N. Ratel-Ramond, J. Plewa, R. Pellenq, M. Monthieux, *C* **2019**, *5*, 69.
- [42] R. Wang, Y. Li, Y.-L. He, *J. Mater. Chem. A* **2019**, *7*, 10962.
- [43] G. Wang, C. Feng, *Polymers* **2017**, *9*.
- [44] R. I. R. Blyth, H. Buqa, F. P. Netzer, M. G. Ramsey, J. O. Besenhard, P. Golob, M. Winter, *Appl. Surf. Sci.* **2000**, *167*, 99.
- [45] F. G. Pacheco, A. A. C. Cotta, H. F. Gorgulho, A. P. Santos, W. A. A. Macedo, C. A. Furtado, *Appl. Surf. Sci.* **2015**, *357*, 1015.
- [46] Z. He, L. Liu, C. Gao, Z. Zhou, X. Liang, Y. Lei, Z. He, S. Liu, *RSC Adv.* **2013**, *3*, 19774.
- [47] C. Gao, N. Wang, S. Peng, S. Liu, Y. Lei, X. Liang, S. Zeng, H. Zi, *Electrochim. Acta* **2013**, *88*, 193.
- [48] M. Park, J. Ryu, Y. Kim, J. Cho, *Energy Environ. Sci.* **2014**, *7*, 3727.
- [49] A. Gaunand, F. Coeuret, *Electrochim. Acta* **1978**, *23*, 1197.
- [50] A. Gaunand, D. Hutin, F. Coeuret, *Electrochim. Acta* **1977**, *22*, 93.
- [51] R. Banerjee, N. Bevilacqua, A. Mohseninia, B. Wiedemann, F. Wilhelm, J. Scholta, R. Zeis, *J. Energy Storage* **2019**, *26*, 100997.
- [52] A. Kossenko, S. Lugovskoy, M. Averbukh, *Materials* **2018**, *11*.
- [53] T.-C. Chang, J.-P. Zhang, Y.-K. Fuh, *J. Power Sources* **2014**, *245*, 66.
- [54] J. González-García, P. Bonete, E. Expósito, V. Montiel, A. Aldaz, R. Torregrosa-Maciá, *J. Mater. Chem.* **1999**, *9*, 419.
- [55] L. Gao, H. Lu, H. Lin, X. Sun, J. Xu, D. Liu, Y. Li, *Chem. Res. Chin. Univ.* **2014**, *30*, 441.
- [56] W. Li, Z. Zhang, Y. Tang, H. Bian, T.-W. Ng, W. Zhang, C.-S. Lee, *Adv. Sci.* **2016**, *3*, 1500276.
- [57] R. J. Rice, R. L. McCreery, *Anal. Chem.* **1989**, *61*, 1637.
- [58] A. Peigney, C. Laurent, E. Flahaut, R. R. Bacsa, A. Rousset, *Carbon* **2001**, *39*, 507.
- [59] R. Subbaraman, D. Tripkovic, K.-C. Chang, D. Strmcnik, A. P. Paulikas, P. Hirunsit, M. Chan, J. Greeley, V. Stamenkovic, N. M. Markovic, *Nat. Mater.* **2012**, *11*, 550.
- [60] F. Dionigi, P. Strasser, *Adv. Energy Mater.* **2016**, *6*, 1600621.
- [61] D. Y. Chung, P. P. Lopes, P. Farinazzo Bergamo Dias Martins, H. He, T. Kawaguchi, P. Zapol, H. You, D. Tripkovic, D. Strmcnik, Y. Zhu, S. Seifert, S. Lee, V. R. Stamenkovic, N. M. Markovic, *Nat. Energy* **2020**, *5*, 222.
- [62] M. E. Lee, H.-J. Jin, Y. S. Yun, *RSC Adv.* **2017**, *7*, 43227.
- [63] L. Dong, F. Hou, X. Zhong, R. Wang, J. Chen, L. Wang, *Compos. Part A Appl. Sci. Manuf.* **2013**, *55*, 74.
- [64] G. Lou, Y. Wu, X. Zhu, Y. Lu, S. Yu, C. Yang, H. Chen, C. Guan, L. Li, Z. Shen, *ACS Appl. Mater. Interfaces* **2018**, *10*, 42503.
- [65] R. E. G. Smith, T. J. Davies, N. d. B. Baynes, R. J. Nichols, *J. Electroanal. Chem.* **2015**, *747*, 29.

Manuscript received: October 28, 2020

Revised manuscript received: November 12, 2020

Accepted manuscript online: November 21, 2020